BAR-ILAN UNIVERSITY

Spintronics with magnetic domains in SrRuO$_3$

MICHAEL FEIGENSON

Ph.D. Thesis
Submitted to the Senate of Bar-Ilan University

Ramat-Gan, Israel   2008

This work was carried out under the supervision of

Professor Lior Klein

Department of Physics

Bar-Ilan University

Acknowledgments

I am very grateful to all those who have helped me over the past years as I worked on my doctorate. I thank my advisor, Lior Klein, for introducing me to the fascinating world of Spintronics and for accompanying me during six years of graduate studies. Lior's uncompromising professionalism and vision were of great inspiration to me.

I thank my collaborators, who over the years became my good friends. To Isaschar Genish, who has extraordinary experimental skills, for his constant willingness to help and for giving me a very extensive introduction to SEM. To Yossi Bason, who always made sure that the computer facilities in our lab worked with Swiss precision, for his help in programming Keithley instruments. To Moty Schultz, who during the last five years dedicated enormous efforts to changing my views about politics, electric switches and life in general, for teaching me a great deal about self-humor.

Ishai Shperber, Nati Naftalis and Snir Seri, who joined our laboratory in the last years, helped create a great atmosphere, and I thank them for that. I am grateful to Liora Bitton, who spent long hours working with me on e-beam lithography and to Jim Reiner, whose excellent samples of $SrRuO_3$ were indispensable to my research. I am also grateful to my good friend Pearl Kaplan for trying to read physics and edit my English.

Finally, I thank my family who gave me their full love and support over the years, even though it meant giving up their dream of seeing me play violin in the Grand Hall of the Moscow Conservatory.

Contents

Abstract

Spintronics is a new and evolving field of science, that makes use of the magnetic properties of materials together with their electric properties to create a new generation of the electronic devices. One of the major challenges of Spintronics is the ability to manipulate magnetic structures down to the nanoscale. The primary method of manipulation used in the existing spintronic devices, such as Magnetic Random Access Memory, is by current generated magnetic field. This method, however, suffers from two major drawbacks: nonlocality and lack of scaling. For these reasons there is an extensive effort to find other methods of manipulation that will not suffer from those drawbacks. One promising method, which is both local and scalable, is current-induces magnetization dynamics. Two major effects are considered in this respect: current-induced switching and current-induced domain wall motion. Both effects have been extensively studied in recent years in Permaloy and Co/Cu multilayers. The domain wall width in those materials is quite thick: $\sim 150nm$ in Permaloy and $10nm$ in Cobalt.

In this work I studied the current-induced domain wall motion in $SrRuO_3$ which is an excellent example of the ultrathin domain wall limit. $SrRuO_3$ is a 4-d itinerant ferromagnet with domain structures in the form of stripes. The width of the domain walls in this compound is only $\sim 3nm$. I demonstrated that the domain walls in

$SrRuO_3$ can be displaced with very high efficiency and with very modest current densities of $10^9 - 10^{10}$ A/m^2. This current density is two orders of magnitude less than typical current density in other metallic systems.

These results are particularly significant in industrial applications, because one can artificially create thin domain walls in soft magnetic materials like Permaloy and thereby significantly decrease their critical current density. This research was published in Physical Review Letters **98**, 247204 (2007).

In additional to current-induced domain wall motion, I studied another effect, which as we believe related to current-induces nucleation. We found that even when $SrRuO_3$ is fully magnetized with no domain walls present, high enough current pulses can destabilize the magnetic state of the film. From comparison of those results with our previous results of current-induced domain wall motion, we showed that those two phenomenon have different origin. This study was recently published in Journal of Applied Physics **103**, 7 (2008).

My third project was a study of the magnetic pinning of vortices in the Super-conducting/Feromagnetic (SC/FM) multilayers. When the ferromagnetic film is in its domain state, it induces inhomogeneous distribution of magnetic fields in the superconducting layer. This may lead to an increase of the pinning of the vortices and hence to an increase of the superconducting critical current. In the current work, I studied the effect of the domain structure in the $Nb/SrRuO_3$ multilayer on the critical current of Nb with current flowing perpendicularly to the domains. I found that in this configuration the ferromagnetic domain structure decreases the critical current. This study was published in the Journal of Applied Physics **97**, 10J120 (2005).

Chapter 1

Scientific Background

1.1   Itinerant Ferromagnetism

Most materials in the periodic table exhibit magnetic properties. The value of the magnetic moment is originated in how electronic levels are filled in an open atomic shell. This property is defined by three Hund's rules.

We can distinguish between two types of magnetism, itinerant and localized, dependent on the nature of participating electrons. Localized magnetism is caused by electron that are attached to the atom and it is described by atomic theory [1]. Itinerant magnetism is caused by conduction electrons and it is the result of strong electron interaction.

A prominent example of an itinerant-metallic system is a 3d ferromagnets with 3d electrons responsible for the magnetic properties. In a 3d band, a maximum of ten electrons per atom can be populated (five electrons with spin up and five electrons with spin down). For example, in Copper (Cu) metal there are ten 3d electrons and the 3d band is completely filled. The filled energy band cannot contribute a magnetic moment because the two electrons on each level have opposite spin and thus cancel each other out. However, in other 3d metals there are less 3d electrons in the atom
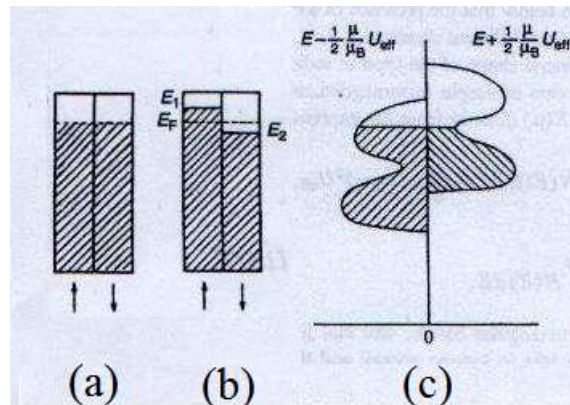
Figure 1.1: Schematic picture of the partially filled energy band with a) balanced and b) unbalanced spins. c) Relative position of the two 3d half bands with opposite spin direction.

and the 3d band is partially filled. This situation is depicted in Figure 1.1a and b, where, for the sake of simplicity, 3d bands are presented as rectangular bands. If both types of electrons are presented in equal amounts, there will not be a magnetic moment associated with the 3d band (Figure 1.1a). However, this situation is not always stable.

Electrons can gain energy by reversing their spin from an antiparallel to a parallel state. As a result, an imbalance between the spin-down subband and the spin-up subband is created (Figure 1.1b). The force creating this spin imbalance is the exchange force. During the reversion one or more electrons is raised to higher energy levels, and therefor the reversion process is counteracted by an increase in the energy of the electrons.

In 1938, Stoner proposed that energy gain due to exchange interaction during spin reversion is given by

$$\Delta E_{ex} = -\frac{1}{4}Jm^2 \tag{1.1}$$

where J is exchange integral and $m = n_\uparrow - n_\downarrow$ is the number of excess electrons with specific spin. $n_\uparrow$ and $n_\downarrow$ are the numbers of electrons per atom for each spin state and the magnetic moment of the atom is given by $\mu = m\mu_B$.

The decrease in exchange energy is accompanied by an increase in kinetic energy, ΔE_K, which is necessary to feel the states of higher kinetic energy in the band. The increase in kinetic-energy can be written as

$$\Delta E_K = \frac{1}{4}\frac{m^2}{N(E_F)} \tag{1.2}$$

where $N(E_F)$ is the density of states at the Fermi energy level.

The total energy variation due to spin reversion is

$$\Delta E = \Delta E_K + \Delta E_{ex} = \frac{1}{4}\frac{m^2}{N(E_F)} - \frac{1}{4}Jm^2 = \frac{1}{4N(E_F)}[1 - N(E_F)J]m^2 \tag{1.3}$$

Examination of the energy band shows that there can be spontaneous magnetization (m not vanishing) when

$$JN(E_F) > 1 \tag{1.4}$$

This condition is the *Stoner criterion* for ferromagnetism. It favors a strong electron-electron interaction and large density of states. This criterion is roughly satisfied in the case of Fe, Co and Ni. The density of states of s and p-electrons bands is considerably smaller than that of the d band, which explains why band magnetism is restricted to elements that have a partially empty d band.

Figure 1.1c demonstrates a more general band shape. Since it is unphysical to have Fermi energy at a higher level in a majority electron band than in a minority electron band, the electron band diagrams usually presented with the two subbands shifted relative to each other after electron transfer.

1.2   Magnetic Phenomena

1.2.1   Magnetic Anisotropy

The dependence of the magnetic properties of the materials on the direction of their measurement is called magnetic anisotropy. There are several types of anisotropy: magnetocrystalline anisotropy, shape anisotropy, stress anisotropy, exchange anisotropy, and more. In this chapter, I will consider the origins of magnetocrystalline and shape anisotropy.

Magnetocrystalline Anisotropy

When ferromagnetic material is spontaneously magnetized, the direction of the saturated magnetization is parallel to the *easy-axis of magnetization*. A relatively small magnetic field is required to magnetize a sample in the direction of the easy axis, however, a fairly large field is required to rotate the domains in other directions. The force which tends to bind magnetization in a certain direction relative to the crystal axis is called *magneto-crystallin anisotropy*. Since the magnetic field works against the anisotropy field, energy is stored in the crystal when magnetization points not in the direction of the easy axis. This energy is a called *magneto-crystallin anisotropy energy*. In a cubic crystal this energy is defined as

$$E_{an} = K_0 + K_1(\alpha_1^2 \alpha_2^2 + \alpha_2^2 \alpha_3^2 + \alpha_3^2 \alpha_1^2) + K_2(\alpha_1^2 \alpha_2^2 \alpha_3^2) + \dots \tag{1.5}$$

where $K_0, K_1, K_2...$ are anisotropy constants and α_1, α_2 and α_3 are the cosines of the angles between the magnetization and the crystal axis. When K_2 is zero, the direction of the easy axis of magnetization is determined by the sign of K_1. If K_1 is positive, then $E_{100} < E_{110} < E_{111}$. In this case, the direction of the easy-axis is

$< 100 >$, since anisotropy energy is minimum when the magnetization points in this direction. If K_1 is negative, then $E_{111} < E_{110} < E_{100}$ and $< 111 >$ is the direction of the easy-axis. When K_2 is not zero, both K_1 and K_2 define the direction of the easy-axis.

In a hexagonal crystal, the hexagonal c axis is the direction of the easy magnetization and the anisotropy energy depends only on the angle μ between the saturation magnetization and the c axis of the crystal. In this case

$$E_{an} = K_0 + K_1 sin^2\mu + K_2 sin^4\mu + ::: \tag{1.6}$$

The anisotropy that makes the magnetization point up or down along a single easy axis, is called *uniaxial anisotropy*.

The physical origin of the crystal anisotropy is the spin-orbit coupling. The electron orbits of the electron are strongly fixed to the atom due to the very strong orbit-lattice coupling. Thus, when an external magnetic field tries to reorient the spin of an electron, the orbit of that electron also tends to be reoriented because of a coupling between the spin and the orbit motion of the electron. The strength of the anisotropy in the atom is measured by the anisotropy constants.

Shape Anisotropy

When a sample has no preferred orientation of magnetization it has no crystalline anisotropy. If such a sample has a nonspherical shape, it is much easier to magnetize it along a long axis than along a short axis. This phenomenon is called *magnetic shape anisotropy*. Its origin is the magnetic free poles that form at the ends of the specimen and give rise to a large demagnetization field that opposes the magnetization (Figure
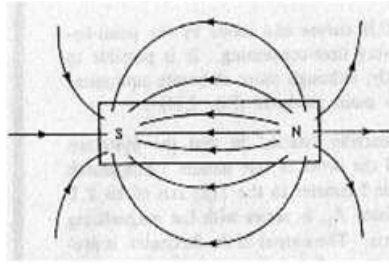
Figure 1.2: The demagnetization field of the bar magnet that opposes the magnetization.

1.2). The demagnetizing field along the short axis is much stronger than that along the long axis, therefore it is necessary to apply much higher magnetic field along the short axis to magnetize the sample to the same extent. The magneto-static energy associated with this field equals to

$$E_{ms} = \frac{1}{2} N_d M^2 \tag{1.7}$$

where N_d is the demagnetizing coefficient, which depends on the shape of the sample, and M is the saturated magnetization.

1.2.2 Magnetic Domains

A uniformly magnetized specimen has a very large magneto-static energy (Figure 1.3 a). This energy can be significantly decreased if the sample splits into domains where magnetization points in opposite directions (Figure 1.3 b,c). The splitting brings the north and south poles closer to each other, thus decreasing the extent of the H field. However, the division into small domains is limited, as each newly created domain adds energy into the system.

A more significant reduction of energy is possible when the lines of the magnetic flux close inside the sample, creating what is called *closure domains* (Figure
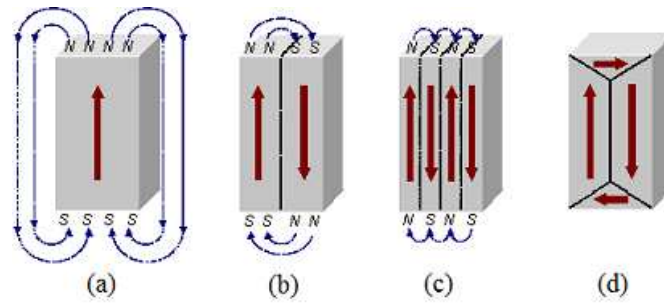
Figure 1.3: Schematic picture of the magnetic domains. A single-domain ferromagnetic material (a) splits into smaller domains (b),(c) in order to reduce the magneto-static energy. (d) The closure domains reduce the magneto-static energy even more by closing the magnetic flux lines inside the sample.

1.3 d). Closure domains can occur in a uniaxial crystal when the magnetocrystalline anisotropy is not too large. In this case the magnetization flux deviates from the direction of the easy-axis near the surface and prevents the formation of free poles. The competition between reduction of the magneto-static energy and anisotropy energy is characterized by the parameter Q, defined as $Q = \frac{K_1}{2\pi M_s^2}$, where K_1 is the anisotropy constant and M_s is the saturation magnetization. Closure domains are created in the specimen when $Q \ll 1$, namely, when the contribution of magneto-static energy is much higher than the contribution of the anisotropy energy.

1.2.3 Magnetic Domain Walls

Spontaneous magnetization changes gradually between two neighboring domains (Figure 1.4) and the transition region is called a *magnetic domain wall* (DW). Two factors affect the width of the DW: the anisotropic energy and the exchange energy. The exchange energy is defined as
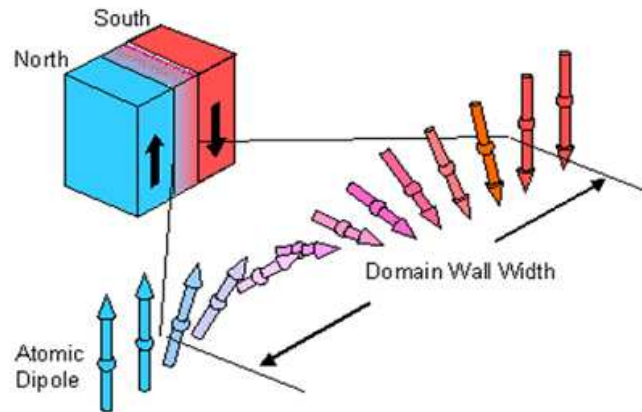
Figure 1.4: Schematic picture of the magnetic domain wall.

$$E_{ex} = -JS^2 cos\mu \qquad (1.8)$$

where J is exchange integral, S is spin quantum number and μ is the angle between two neighboring spins. In ferromagnetic materials, a minimum of exchange energy is achieved when two spins are parallel. When spins deviate from the parallel state, the variation in the exchange energy is

$$\Delta E_{ex} = -JS^2\mu \qquad (1.9)$$

and therefore the exchange energy of the wall is reduced when spins change their orientation over N atoms by small angles. To calculate E_{ex} per area of the wall, we assume that the atoms are located at the corners of the cubic lattice with a width a. For a wall of 180^0, $\mu = \frac{180}{N}$ and the exchange energy per wall area is

$$\Delta E_{ex} = \frac{JS^2 \mu^2}{Na^2} \qquad (1.10)$$

One can see, that as the width of the wall goes to infinity ($N \to \infty$), E_{ex} vanishes.

The anisotropic energy tends to align each spin in the direction of the easy-axis, and contrary to the exchange energy, to decrease the number of spins in the wall. The anisotropic energy per wall area is proportional to the anisotropy constant K_1, and is defined as

$$\Delta E_{an} = K_1 N a \tag{1.11}$$

Equilibrium is achieved when the increase in anisotropy energy is balanced by decrease in exchange energy. The total energy of the wall with thickness $\delta = Na$ is then given by

$$E_{wall} = \Delta E_{ex} + \Delta E_{an} = \frac{J S^2 \pi^2}{\delta a} + K_1 \delta \tag{1.12}$$

To reduce the total energy of the wall,

$$\frac{\partial E_{wall}}{\partial \delta} = -\frac{J S^2 \pi^2}{\delta^2} + K_1 = 0 \tag{1.13}$$

one can define the width of the wall as

$$\delta = \sqrt{\frac{J S^2 \pi^2}{K_1 a}} \tag{1.14}$$

The values of δ calculated from this formula are 100 nm for Ni, 15 nm for Co, and 3 nm for $SrRuO_3$.

1.3   Spintronics

1.3.1   Giant Magnetoresistance

Spintronics, also known as magneto-electronics, is a rapidly evolving field of science that employs the magnetic properties of materials, together with their electric properties, to create a new generation of electronic devices. The origin of Spintronics is attributed to two research groups led by Albert Fert and Peter Grunberg, who independently discovered a new effect in 1988, which they called Giant Magneto Resistance (GMR) [2, 3]. The GMR effect was first discovered in Fe/Cr/Fe multilayers at low temperatures and in a high magnetic field. In the multilayer, two ferromagnetic layers are separated by a non-magnetic layer. The GMR effect is measured when the magnetic orientation of one of the layers is switched through the application of a magnetic field (Figure 1.5). When the magnetization of two layers are parallel, the spins of one orientation have lower average resistance; they carry more current thus lowering total resistance of the structure as compared to the situation when the magnetization of the layers is anti-parallel. When the two ferromagnetic layers are separated by the insulating layer, instead of the non-magnetic layer, the effect is called Tunneling Magneto Resistance (TMR). Due to the large difference in resistance, the application potential of GMR was immediately recognized. The discovery of GMR in Co/Cu multi-layers at room temperature and small magnetic fields a few years later [4] finally made GMR a technological reality.

Since the late 1990's, IBM has been incorporating GMR and TMR devices into read-head sensors for magnetic disk drives. The very high sensitivity of GMR enabled radical miniaturization of the hard disks, and today it is a standard technology for
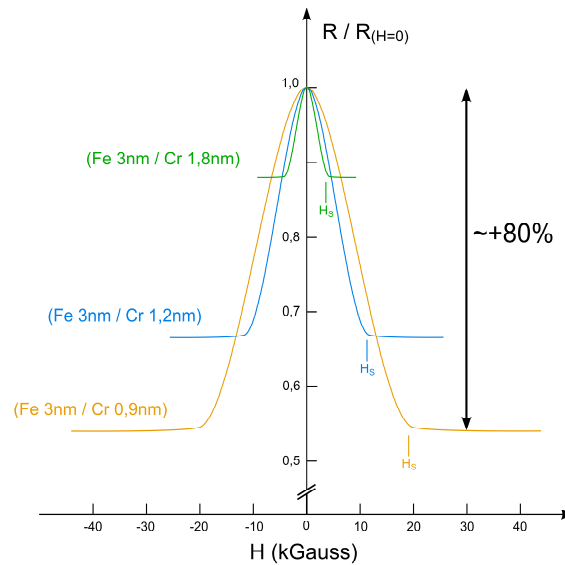
Figure 1.5: GMR measurements in Fe/Cr/Fe multilayer for three thicknesses of the Cr layer [2].

read-out heads. In 2007, Albert Fert and Peter Grunberg received a Nobel prize in Physics for their discovery of GMR.

1.3.2 Magnetoresistive Random Access Memory - MRAM

MRAM is a novel computer memory technology based on the TMR effect. Each TMR cell formatted from two ferromagnetic layers is separated by an insulating layer. One of the magnetic layers is a permanent magnet with the magnetization set to a specific polarity, while the magnetization of another magnetic layer is free to rotate. The reading of stored data is performed by measuring the TMR effect across the plates. When the plates have a similar polarity, it is considered as "0"; when the polarity is different it is considered as "1" (Figure 1.6). A memory device is built from the grid of such cells.

To write data in a memory cell it is necessary to manipulate the free magnetic
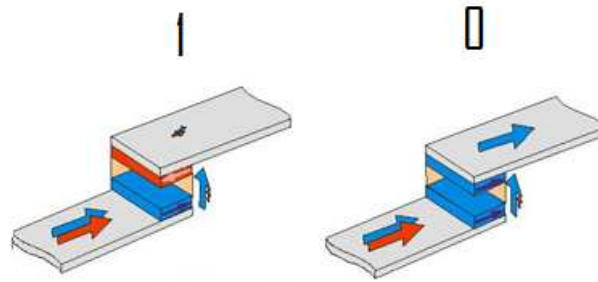
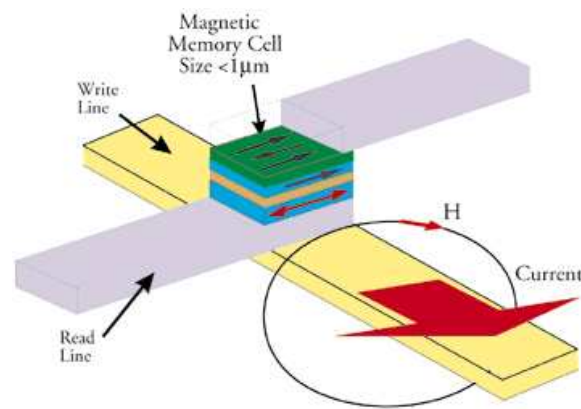Figure 1.6: MRAM memory cell based on the TMR effect.

Figure 1.7: MRAM device with field induced switching.

layer. The main method of manipulation in the existing MRAM devices is using a current generating magnetic field (Figure 1.7). However, this method suffers from two major drawbacks: *non-locality* and *scaling*. With non-locality, as the device is scaled down in size, the induced field in one unit cell may affect a neighboring unit cell leading to potential false writes. This limits cell sizes to around 180 nm. With scaling, the current needed for the operation of the device does not decrease with decreasing cell size, therefore the current density and heating increase. To compensate for these drawbacks there is an intensive effort to find other ways of manipulation.

A promising method that is both local and scalable is Current-Induced Magnetiza-

tion Dynamics (CIMD). CIMD can radically decrease switching currents and energy consumption per bit write. The manipulation of the free magnetic layer by use of an electric current can significantly improve the performance of MRAM and make it a truly universal memory.
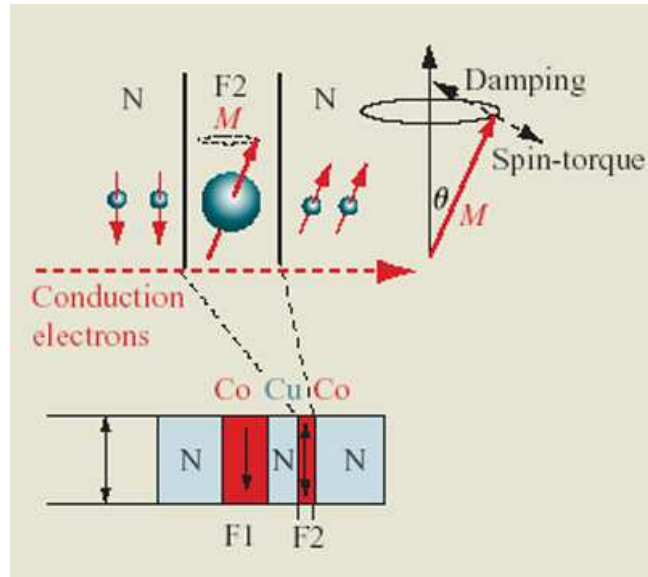
Figure 1.8: Schematic picture of the spin momentum transfer in the ferromagnet (F1)/normal (N)/ferromagnet (F2) multilayer. While crossing the first ferromagnetic layer (F1), the electron spins become spin-polarized. When reaching the second ferromagnetic layer (F2) magnetized in the opposite direction, they exert a torque on that layer, leading to precession of the localized magnetization or to the magnetization switching.

1.4   Current-Induced Magnetization Dynamics

Current-Induced Magnetization Dynamics recently raised an extensive interest from the view point of the spintronic applications. Two main effects are mentioned in this respect. One effect, discussed by Slonczewski [6], is the interaction between spin-polarized current injected into an ultrathin magnetic region and the magnetic moment of that region. This interaction leads to two possible phenomenon: a steady precession of the localized magnetization driven by a constant current (for $I < I_c$) and the switching of the thin magnetic region driven by a pulsed current (for $I \geq I_c$) (Figure 1.8). Both magnetization switching and a signatures of spin precession have
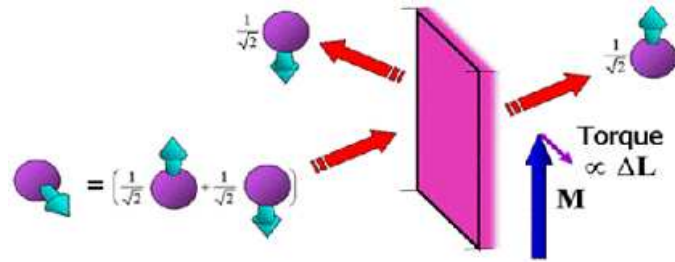
Figure 1.9: Linear momentum transfer.

been reported in Co/Cu/Co pillars and multilayers [7, 9, 10].

Another effect of CIMD, first proposed by Berger [11], is the interaction between spin-polarized current and a ferromagnetic domain wall, which leads to wall displacement. More recent theories suggest that conduction electrons affect the domain wall motion in two ways [22]. The first way is momentum transfer, due to the reflection of the conduction electrons. When electrons scatter from the DW interface the reflection amplitudes are different for the majority and the minority electrons. As a result, the spin component transverse to the magnetization is reduced. To keep the total angular momentum between the incoming and the outgoing states, the moment of the reflected electrons is absorbed by the magnetization of the ferromagnet and the force is applied on magnetization of the ferromagnetic material (Figure 1.9). This effect is proportional to charge current and wall resistance and hence is significant in thin walls.

The second way is the spin torque transfer, which appears when the electrons pass through the wall. This effect is dominant in thick walls where the spin orientation follows the magnetization of the wall.

Current-induced DW motion was extensively studied in multilayers and pattered

constrictions of Permalloy [14, 13, 15, 16], Co [8], MnGaAs [18]. Different techniques were used for detection and observation, such as magneto-optics [16, 18], magnetic force microscopy [9, 13], change in resistance of spin valve structures [14, 15], change in longitudinal resistance [12, 20] and Hall effect [18]. The typical current density for DW displacement achieved in the metallic systems is in the range of $10^{11} - 10^{12}$ A/m^2. In my work, I studied current-induced domain wall displacement in $SrRuO_3$ and showed that the DW's in this compound can be displaced with relatively modest current densities of $10^9 - 10^{10}$ A/m^2. Similar results were only achieved in the ferromagnetic semiconductor [18] or in metallic systems with the assistance of an external magnetic field [21].

The theoretical study of current-induced DW motion in the limit of ultrathin DW's was presented by Tatara and Kohno [22]. They found that the depining current density is inverse proportional to the wall resistivity $\hbar_w$, $j^{cr} \propto V_o/\hbar_w$, where V_o is the pining potential, and it is written as

$$ j^{cr} = \frac{2 H_c \mu_B}{e n a^3 R_w A} \tag{1.15} $$

where H_c is the critical depining field, R_w is the wall resistance, A is the cross section area, n is the electron density and a is the lattice constant.

In addition to current-induced switching and current-induced domain wall motion, a third effect of the interaction between the spin current and the ferromagnetic layer was recently proposed. It was suggested that when a spin-polarized current applied to the uniformly magnetized ferromagnetic film exceeds a certain critical value, it can lead to the destabilization of the uniform ferromagnetic state and to the nucleation of the magnetic domains [23]. Recent experimental observations of the domain formation

in metallic and semiconducting pillars and films are believed to be related to this effect [24, 25, 26, 27]. In this work, we present experimental data on destabilization of the magnetic state in the uniformly magnetized layer of $SrRuO_3$ [28]. We believe that these results are related to current-induced nucleation.
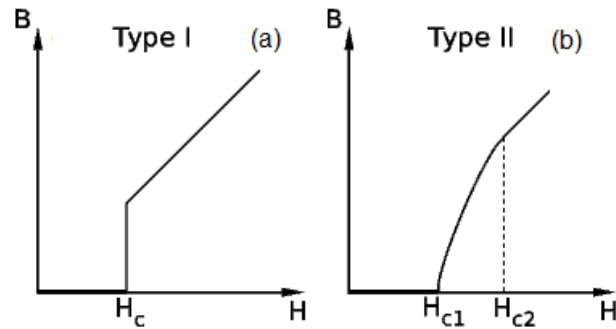
Figure 1.10: B vs H at type I (a) and type II (b) superconductors.

1.5 Superconductivity

1.5.1 Types of Superconductors

Superconductivity is a phase of material that occurs in certain metals under a certain critical temperature, T_c. Superconductivity is characterized by zero electric resistance and by the exclusion of an inner magnetic field (Meissner effect). There are two types of superconductors: type I and type II. In type I superconductors, a relatively small magnetic field totally expelled from the material. Above a certain critical field, H_c, the magnetic field penetrates the material completely and destroys the superconductivity (Figure 1.10 a). In type II superconductors there are three stages: for $H < H_{c1}$ there is a Meissner effect and the magnetic field is totaly expelled from the material, for $H_{c1} < H < H_{c2}$ the material is still a superconductor but there is partial penetration of the magnetic field in the form of vortices - quantized lines of magnetic flux, and for $H > H_{c2}$ there is total penetration of the magnetic field while the material behaves as a normal metal (Figure 1.10 b).

1.5.2 Vortex Pinning

When there is partial penetration of the magnetic field into a superconductor, the current applies force on the vortices, which leads to their motion perpendicular to the direction of the current (Figure 1.11). The change in the magnetic flux Φ due to the motion of the vortices induces an electric field inside the material, $E = \frac{\partial \Phi}{\partial t}$ .This field leads to the energy dissipation, $P = E \cdot J$, which is equivalent to resistivity.

The highest current that can flow in a superconductor without initiating the motion of the vortices is called critical current, J_c, and it is dependent on temperature and magnetic field. One can significantly increase J_c by increasing the pinning of the vortices. For example, the pinning can be increased by creating microscopic defects, which locally suppress superconductivity. It is favorable for vortex normal core to be located in the area which is normal anyway, thus saving condensation energy. Using this method one only tries to pin vortex normal core, which is relatively small, especially at high T_c materials ($\xi \sim 3nm$) [5]. The pinning energy in this case is the condensation energy of the Cooper pair in the normal volume of the vortex core, $U_{cp} \sim [\frac{H_c^2}{8\pi} \frac{1}{4} \xi^2] = [\frac{\Phi_0}{8\pi\lambda_L}]^2$, where H_c is the thermodynamic critical field, ξ is the radius of the core (the superconducting correlation length), Φ_0 is the flux quantum and λ_L is the London penetration length. U_{cp} drops significantly as the temperature approaches T_c because of the increase of the λ_L.

Recently, it was proposed to pin the vortex flux instead of its normal core. This type of pinning can be achieved in the ferromagnet - superconductor (FM/SC) multilayer [29, 30], where the magnetic flux of the vortex is pinned by the magnetostatic interaction between magnetic flux of the vortex and magnetization of the FM layer.
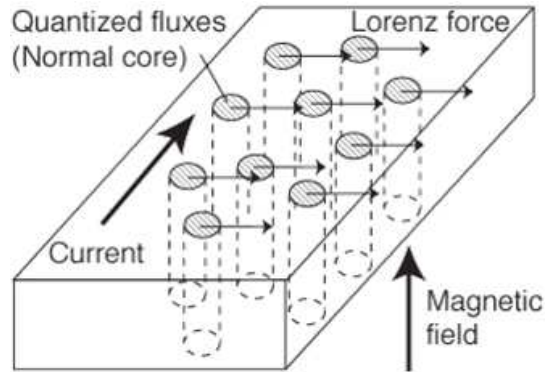
Figure 1.11: Lorentz force acting on the vortices, leads to their motion perpendicular to the current.

In this type of vortex pinning the pinning potential is defined as $U_{mp} = \Phi_0 M d_s$, where M(x) is the magnetization of the FM layer and d_s is the thickness of the SC. This pinning energy does not depend on temperature when the bi-layer is under the Curie temperature of the FM layer, although the depinning energy still depends on temperature.

1.5.3 FM/SC Multilayer

In the FM/SC multilayer system, the fringing field from the DW's in the FM layer may exceed the critical magnetic field and thus locally destruct superconductivity in a sufficiently thin SC layer (Figure 1.12). As a result, a normal region will be produced in a type I superconductor or a transition to a mixed state will occur in a type II superconductor, where the magnetic flux will penetrate in a form of localized vortices.

To determine the fringing field around the DW's in ferromagnetic material with the easy-axis in the plane of the film, one should solve a magnetostatic problem at the interface between the SC and FM layers and impose a boundary condition that
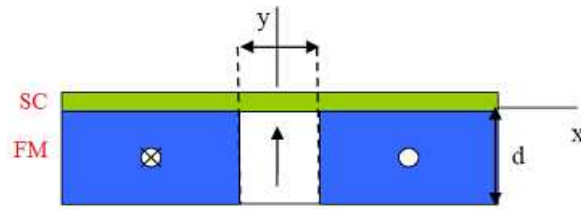
Figure 1.12: FM/SC bi-layer. The magnetic filed generated by the DW's at the interface between two layers can locally suppress superconductivity in the SC layer.
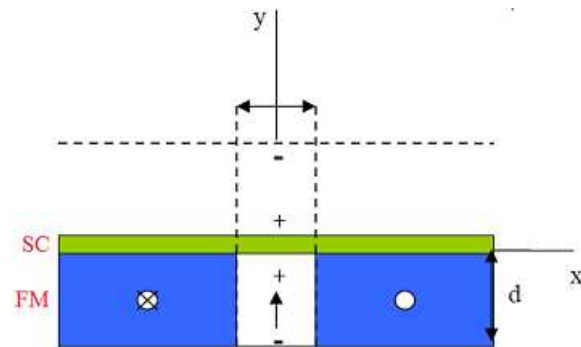

Figure 1.13: Introduction of the image charge imposes the boundary conditions, H=0, at the interface between the layers.

the magnetic field does not penetrate into the SC layer due to the Meissner effect. The solution is conveniently written in the complex form for the magnetic field vector H, where $H = H_x + iH_y$. The normal and the tangential components of the field, H_y and H_x, are expressed by the differentiation of the complex potential by the complex number z

$$\frac{\partial \Omega}{\partial Z} = H_x + H_y \qquad (1.16)$$

while the complex potential is determined by the following relationship

$$\Omega(z) = \Phi(x, y) + i\Psi(x, y) \qquad (1.17)$$

where Φ is a harmonic function satisfying the Laplace equation and Ψ is a conjugate harmonic function. Both, Φ and Ψ satisfy Cauchy - Reimann relationship $[\frac{\partial \Phi}{\partial x} = \frac{\partial \Psi}{\partial y}; \frac{\partial \Phi}{\partial y} = -\frac{\partial \Psi}{\partial x}]$.

By introducing a mirror charge in the region $y > 0$, which imposes the boundary condition $H_y = 0$ (Figure 1.13), the complex potential of the FM/SC by-layer at the presence of the domain wall can be written as

$$\Omega(z) = 4\Delta M ln(x) - 2\Delta M ln(z - id) - 2\Delta M ln(z + id) \qquad (1.18)$$

where M is the magnetization of the material per unit area, Δ is the width of the magnetic domain wall, and d is the thickness of the FM layer. The magnetic field is then determined as

$$
\begin{aligned}
\frac{@\Omega}{@z} &= 2\Delta M[\frac{2}{z} - \frac{1}{z - id} - \frac{1}{z + id}] = \\
&= 2M\Delta[\frac{2x}{x^2 + y^2} - \frac{x}{x^2 + (y - d)^2} - \frac{x}{x^2 + (y + d)^2}] + \\
&\quad + i2M\Delta[\frac{2y}{x^2 + y^2} - \frac{y - d}{x^2 + (y - d)^2} - \frac{y + d}{x^2 + (y + d)^2}]
\end{aligned}
\qquad (1.19)
$$

where x and y are distances from the center of the DW. At the interface between the FM and SC layer (y=0), the field is

$$H_x = 4M\Delta[\frac{1}{x} - \frac{x}{x^2 + d^2}]; H_y = 0 \qquad (1.20)$$

It can be shown, that at the magnetic-bubble geometry, where the direction of the magnetization is normal to the plane of the film, the magnetic field at the interface between two layers is given by

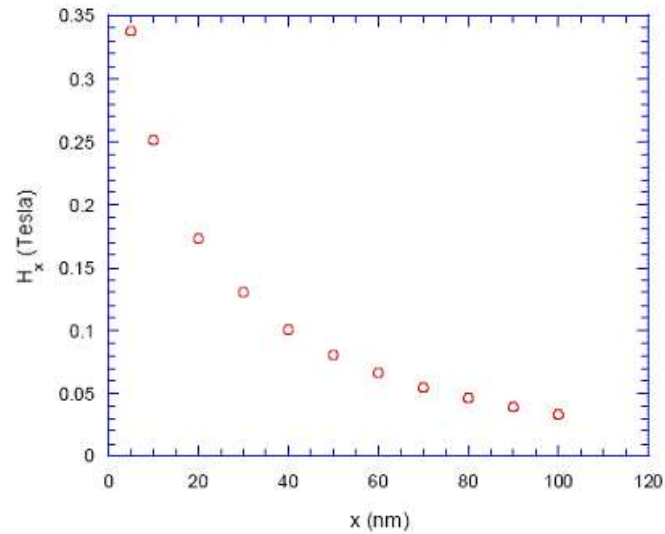$$H_x = 4M ln[\frac{x}{x^2 + d^2}]; H_y = 0 \qquad (1.21)$$

Figure 1.14: Numerical calculation of the fringing magnetic field, H, at the interface between the layers at distance x from the DW.

Figure 1.14 shows the numerical calculation of the magnetic field H_x generated by the single magnetic DW at the interface between the FM and SC layers at distance x from the center of the DW, according to the Ex.1.20. For the FM layer, the data of $SrRuO_3$ was used with a thickness $= 90nm$, $\Delta = 3nm$, magnetization $4\pi M = 0.2T$ and direction of magnetization 60° relative to the film plane. One can see that the magnetic filed of $3500Oe$ is generated at the vicinity of the DW. At the type II superconductor materials, for example Nb where $H_{c2}(T) = 1980Oe$ at T=0 [40], this magnetic filed can be strong enough to weaken the superconductivity and create regions with preferable localization of vortices.

Chapter 2

Materials

2.1   Strontium ruthenate (SrRuO$_3$)

2.1.1   Atomic properties

SrRuO$_3$ is a metallic material with a perovskites chemical structure. The per-ovskites consist of three atoms and have the chemical formula ABO$_3$. One can look at the SrRuO$_3$ as FCC crystal with Ru atoms in the corners, O atoms in the center of the face edges, and the Sr atom in the middle of the cube (Figure 2.1). Due to the large dimensions of the Ru atom, the SrRuO$_3$ has an orthorhombic structure (a=5.53, b=5.57, c=7.82 Å) with the c axis doubled and the a and b axes rotated 45° with respect to the substrate axis (Figure 2.2). The films grown on SrTiO$_3$ substrates can grow with the c-axis in the film plane (along either of the two principal directions of the [001] substrates) or with the c-axis perpendicular to the film plane. The thin films grown on $\sim 2^o$ miscut SrTiO$_3$ substrate grow with the c-axis perpendicular to the miscut direction and in more then 99% of the films the c-axis is pointing in the same direction [32].
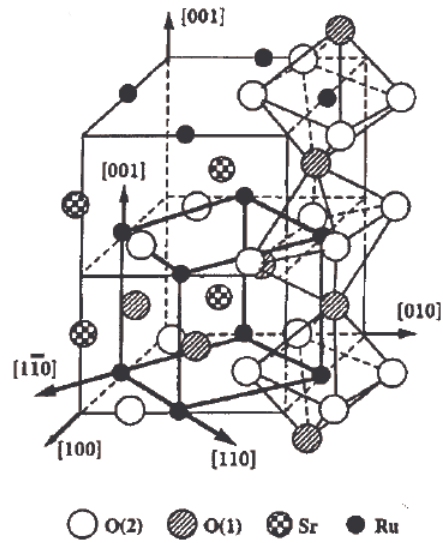
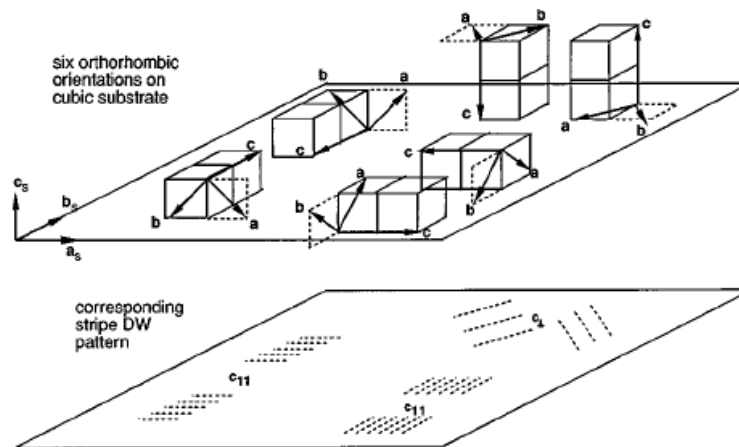Figure 2.1: Schematic picture of the perovskite structure of SrRuO$_3$.

Figure 2.2: Schematic picture of the six crystallographic domain orientations of SrRuO$_3$ and the corresponding magnetic domain orientations [37].
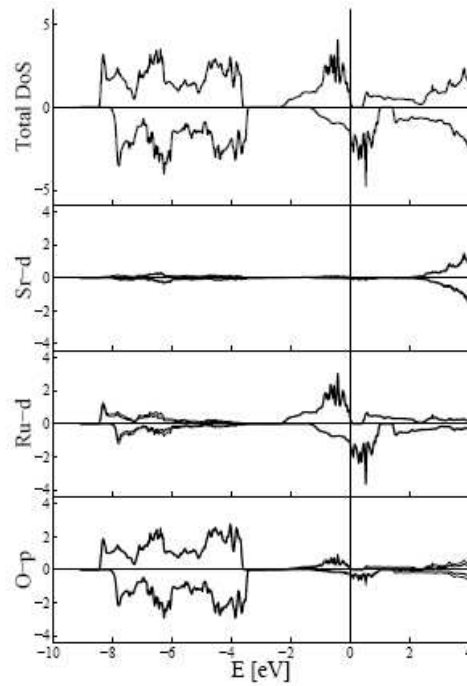
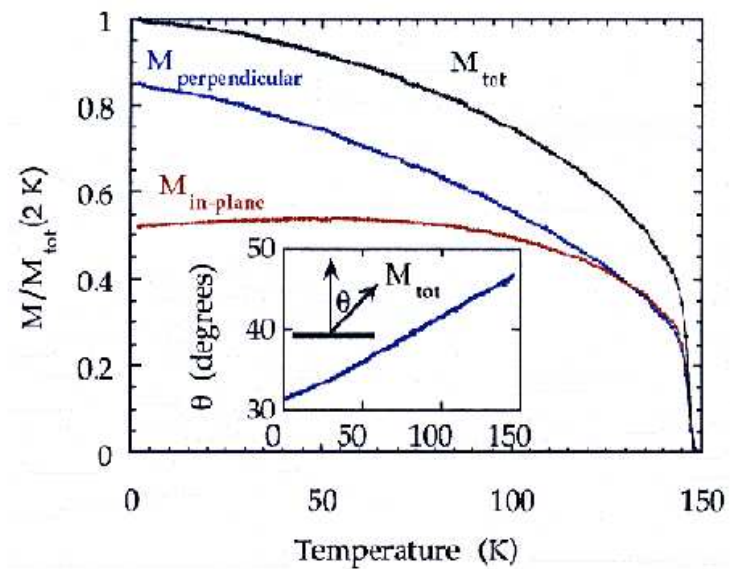Figure 2.3: The total and partial density of state for SrRuO$_3$ [36].

Figure 2.4: Temperature dependence of the in-plane, out-of-plane and total remnant magnetization of the SrRuO$_3$ thin film. Inset: Temperature dependence of the easy direction of the magnetization relative to the normal [32].

2.1.2 Magnetic properties

SrRuO$_3$ is a minority band itinerant ferromagnet with T$_c \sim 150K$ for thin films. The magnetism in this material is dominated by the contribution of the 4d Ru electrons due to their high density of states (Figure 2.3). The magnetic moment of Ru at zero-temperature limit is $1.4\,{}^{\prime}{}_B$ per atom. The easy axis of the magnetization is in the (001) plane and its direction continuously changes relative to the normal from $\sim 45^o$ at T$_c$ to $\sim 30^o$ at low temperatures at a constant rate of $\sim 0.1^o K^{-1}$ (inset of Figure 2.4) [32]. Figure 2.4 shows the temperature dependence of the in-plane and out-of-plane projection of remanent magnetization of the typical SrRuO$_3$ thin film.

2.1.3 Extraordinary Hall Effect (EHE)

Hall resistivity ($\rlap{/}{\rho}_H$) in metals is described as $\rlap{/}{\rho}_H = R_o B + R_s\,{}^{\prime}{}_o M$. The first term ($R_o B$), known as the ordinary Hall coefficient, is present in all metals and describes the influence of the magnetic field on charge carriers. The second term ($R_s\,{}^{\prime}{}_o M$), known as the extraordinary Hall coefficient, is present only in magnetic materials and is proportion to the average component of the magnetization (M) normal to the plane of the film. Figure 2.5 shows the EHE ($R_s\,{}^{\prime}{}_o M$) of SrRuO$_3$ as a function of temperature.

It was shown that R_s behavior in SrRuO$_3$ can not be fit according to the common theoretical prediction as $R_s = a\rlap{/}{\rho} + b\rlap{/}{\rho}^2$, but rather can be described as $R_s = cT^5 + b\rlap{/}{\rho}^2$, where $\rlap{/}{\rho}$ is the longitudinal resistivity, T is the temperature, and a, b and c are constants [35].

The EHE can be used to monitor the magnetic state of ferromagnetic material.
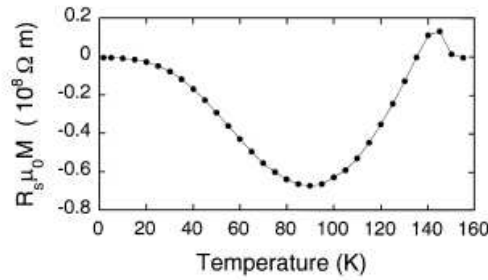
Figure 2.5: The extraordinary Hall effect of SrRuO$_3$ as a function of temperature [35].

It was widely used for this purpose in the current research, as will be explained in Chapter 3.3.

2.1.4 Magnetic domain structures

SrRuO$_3$ thin films exhibit a very large uniaxial magneto-crystalline anisotropy ($\sim 10T$) with the easy-axis of magnetization oriented along the b crystallographic axis. This high anisotropy energy, together with a small self field ($4\pi M = 0.2T$) is responsible for the stripe nature of the domain structures in this compound. Once the domain structures are annihilated by applying a sufficiently large magnetic field, ($\sim 2T$) no new domains renucleate when the field is set back to zero. The Lorentz imaging characteristic study showed that the stripe domain structures, present in all six crystallographic domains, vary in spacing and are at 45° to each other (Figure 2.2) [37]. The high anisotropy energy prevents generation of the closure domains and it also prevents nucleation of the domain structure when the domains are annihilated by allying a strong magnetic field and then setting it to zero.

Figure 2.6 shows the two types of magnetic domains in SrRuO$_3$. The first type, with widely spaced walls, are oriented $\pm 45^o$ relative to the substrate axes with the c
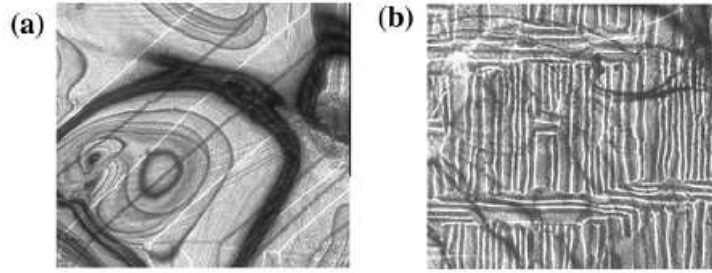
Figure 2.6: The image of the magnetic domain structures in the SrRuO$_3$ thin film taken with the Transmission Electron Microscope in the Lorentz mode: (a) wide domains with the c crystallographic axes normal to the film plane, (b) narrow domains with the c crystallographic axes in the plane of the film [37].

crystallographic axis perpendicular to the substrate and a and b axes in the plane of the film. The domain wall spacing in those domains is on the order of micron and it varies considerably with the thickness of the film (Figure 2.6 a).

The second type of domains, with narrow spaced walls, are oriented parallel to the substrate axis with the c crystallographic axis in the plane of the film and a and b axes pointing out of the plane at 45°. The magneto-static energy in those domains with the magnetization out-of-plane is very high, which leads to a narrow wall spacing of about $200nm$ (Figure 2.6 b).

In our experiments, we used epitaxial SrRuO$_3$ thin films grown on a slightly miscut (2°) SrTiO$_3$ substrate. The films grown on such a substrate grow with narrow spaced Bloch DW's with the easy axis tilted out of the film and the in-plane projection of the magnetization along $[\bar{1}10]$ (Figure 2.7). The calculated width of those DW's according to Eq.1.14 is $\sim 3nm$. The recent study of the SrRuO$_3$/YBa$_2$Cu$_3$O$_7$ bilayer revealed that the superconductor order parameter penetrates the ferromagnet in regions consistent of narrow, less then $8nm$ long stripes, separated by $200nm$ [38].
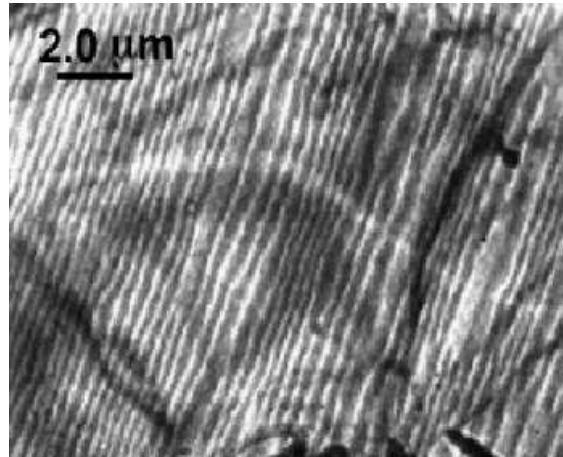
Figure 2.7: The TEM image of the narrow spaced DW's in the $SrRuO_3$ thin film grown on miscut $SrTiO_3$ substrate [37].

This effect was attributed to the proximity effect which takes place along the DW's of $SrRuO_3$. These experimental observation are consistent with the calculated width of the DW's in this materials.

One of the manifestations of the thin width of the DW's in $SrRuO_3$ is its very high interface resistance, $10^{-15}\Omega m^2$. The value of the interface resistance in this compound, deduced from the measurements of the domain wall resistivity, is more then 3 orders of magnitude higher than in Co [39]. This huge difference is believed to be related to the width of the DW's. The width of the DW's in Co is estimated as 5 times larger than in $SrRuO_3$.

2.2 Niobium

Niobium (Nb), also known as Columbium (Cb), was first discovered in 1801. It is a transition metal with the atomic number of 41 and it has a body-centered cubic crystalline structure. When cooled at a low temperatures, Nb becomes a supercon-

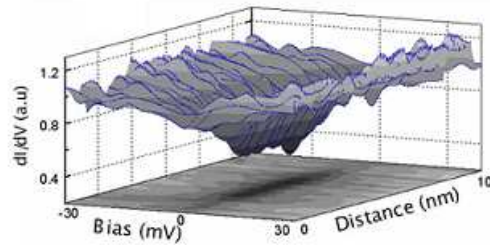Figure 2.8: Tunneling spectra across the domain wall of $SrRuO_3$ in the $SrRuO_3/YBa_2Cu_3O_7$ bilayer. The proximity effect is taking place along the domain walls of $SrRuO_3$. The width of the gaped area is less then 8 nm [38].

Figure 2.9: Niobium.

ductor. Its critical temperature is 9.5 K at atmospheric pressure, which is the highest critical temperature among elemental superconductors. Its critical magnetic field is $H_{c2}(T) = 1980\,Oe$ at $T = 0$[40]. In addition, the magnetic penetration depth of Nb ($\sim 40\,nm$) is the largest magnetic penetration depth among any elements. Nb together with Vanadium (V) and Technetium (Tc), are the only elemental superconductors that are Type II. To keep its superconducting qualities, Nb needs to be kept in a protective environment, as it easily reacts with oxygen and carbon even at moderate temperatures.

Although Nb alloys do not react with human tissue, the reason they are widely used in surgical implants, Nb dust can be toxic and can cause eye and skin irritation.

Chapter 3

Experimental details

3.1 Samples

3.1.1 Growth

In our research, we used high quality epitaxial thin films of $SrRuO_3$ grown on $SrTiO_3$ substrate using *electron beam coevaporation.* At this technology, the electron beam heats the Sr and Ru targets and causes their simultaneous evaporation on the substrate with the presence of oxygen (see a picture of the evaporation system at Figure 3.1).

To create a sample with a single axis of the easy magnetization it is necessary to break a cubic symmetry of the substrate surface. For that reason the substrate was miscut at an angle of 2° (as explained in Chapter 2.1.1). The miscut of the substrate creates atomic steps with a height of $4\mathring{A}$ and a width of $114\mathring{A}$. The $SrRuO_3$ film that grows on such a substrate grows with a uniform direction of magnetization. The average resistivity ratio of 20, measured between room temperature and $4K$, is indicative of the high quality of our samples.

The experiment of the magnetic vortex pinning was done on SC/FM bilayers consisting of an epitaxial thin film of $SrRuO_3$ ($900\mathring{A}$) grown as described above and

Figure 3.1: The electron beam coevaporation system for sample growth.

a thin policrystalline film of Nb ($600\mathring{A}$) grown by sputtering. The layers of $SrRuO_3$ and Nb were separated with a buffer layer of Cu ($20\mathring{A}$) to avoid oxygen migration.

Our $SrRuO_3$ samples were grown by J. W. Reiner at Stanford University in the laboratory of M. R. Beasley and the Nb layers were grown by M. Karpovskiat at Tel-Aviv University in the laboratory of A. Palevsky.

3.2 Patterning

3.2.1 Current-induced DW motion and current-induced nucleation experiments

Due to the stripe nature of the domains in $SrRuO_3$ and due to the fact that the DW orientation is coupled to the miscut direction of the substrate, we were able to fabricate a pattern where we know in advance that the current will flow perpendicular to the DW's. Figure 3.2 presents such a pattern fabricated using e-beam lithography
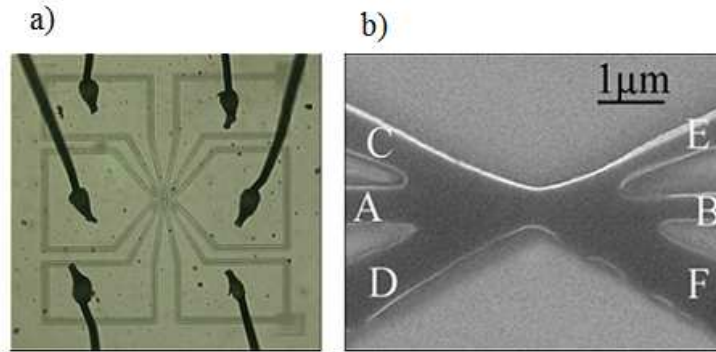
Figure 3.2: The e-beam lithography patterning of $SrRuO_3$ a) the contact pads fabricated in the window of 1000x1000 ^1m b) the "core" of the sample fabricated in the window of 100x100 ^1m.

on a Scanning Electron Microscope (SEM). The form of the pattern enabled us to prepare a state with a single DW located between terminals A and B, and then to manipulate the position of the wall by injecting positive and negative current pulses between terminals A and B. The form of the voltage leads enabled us to monitor the magnetic state of the whole sample by measuring the EHE, which is proportional to the average component of the magnetization perpendicular to the plane of the film (Chapter 2.1.3). The minimum width of the current path in our samples is $\sim 500\mathring{A}$, which is narrow enough to allow injection of the pulses with sufficient current densities and wide enough to prevent damage to the sample from static electricity.

To fabricate a pattern with a resolution of a few hundreds nanometers, the lithography process was performed in two steps. As a first step the contact leads were created in the window of 1000x1000 ^1m (Figure 3.3). At the next step the "core" of the circuite was created in a window of 100x100 ^1m (Figure 3.4). At the final stage of the processing, the sample was etched by ion-mealing in Gatan High-Precession Etching Coating System (HPECS). The description of the processing appears in the
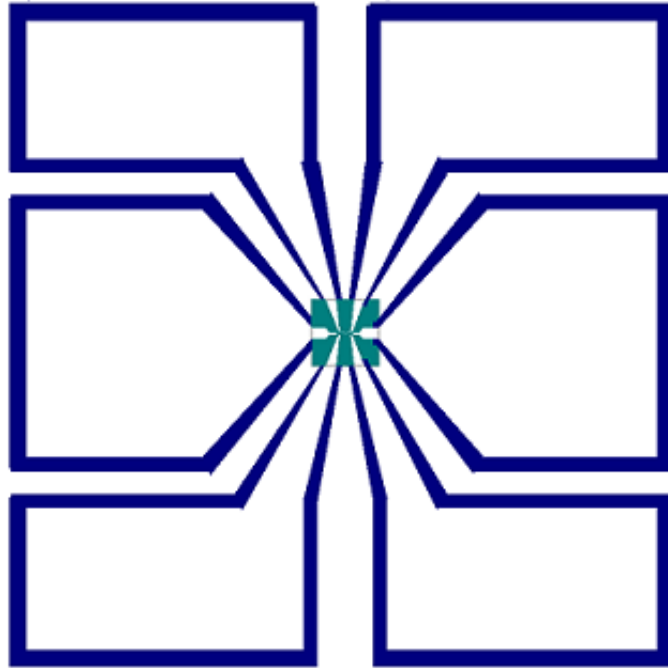
Figure 3.3: The patterning design of 1000x1000 μm. The colored lines show the area where SrRuO$_3$ was removed by etching.

Appendix B.

3.2.2   Magnetic pinning experiment

In the experiment of magnetic pinning with SC/FM bilayers, the pattern was fabricated using UV-lithography, followed by the ion-mealing in Gatan HPECS. We first fabricated a pattern of SrRuO$_3$, which enabled injection of the current perpendicular to the DW's between terminals A and B and the measurement of the voltage between terminals C and D (Figure 3.5). The width of the current path was 50 μm and the distance between the voltage leads was 1000 μm. On top of the SrRuO$_3$ layer we grew a path of Nb with a width of 30 μm, which was patterned using a lift-off technique. The description of the processing appears in Appendix A.

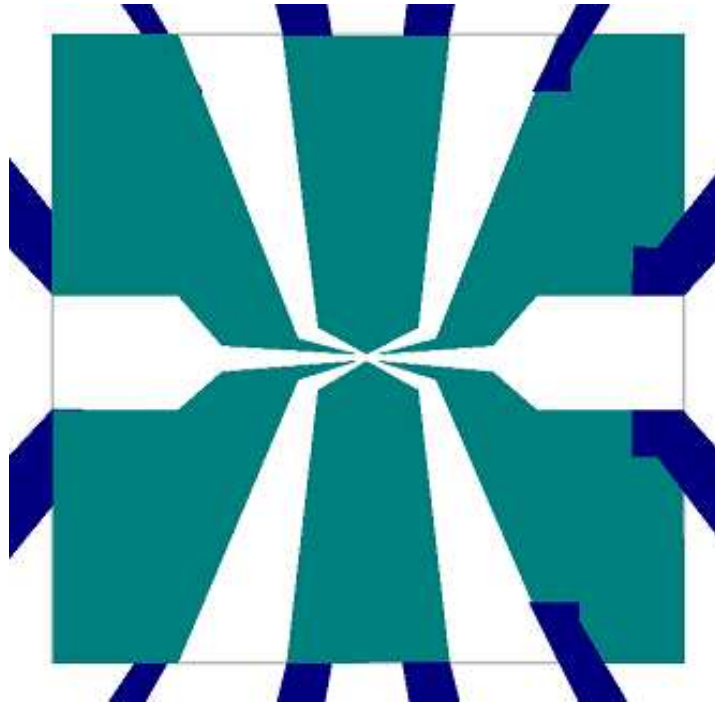Figure 3.4: The patterning design of the "core" of the sample in the 100x100 ^1m window. The colored area was removed by etching at the end of the processing.
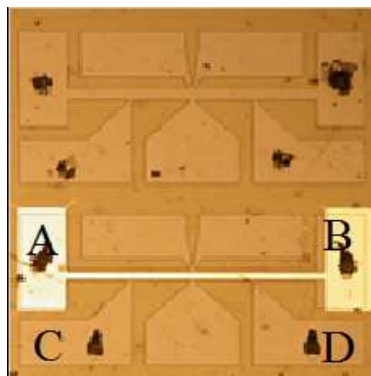

Figure 3.5: The measurement pattern of $SrRuO_3$ with a layer of Nb grown on it.

3.3   Experimental set-up

3.3.1   Measuring system

In this research we used the Quantum Design Physical Properties Measurement System (PPMS), which performs measurements of electric transport and magnetic properties of materials in temperatures between 1.2 and 400K, with a current range of 1 ^1A - 10mA, and which can apply a magnetic fields up to 9T (Figure 3.6).

In the experiment of current-induced DW motion and current-induced nucleation, we used PPMS in order to cool the sample to cryogenic temperatures and to apply magnetic fields. The actual measurements of resistivity and EHE were done using Keitley instruments. All the instruments were programmed on Visual Basic (VB) and they communicated with PPMS through the GPIB protocol (Figure 3.6). The user manual for the measurement system appears in Appendix C. The use of external instruments provided high level of flexibility to inject current and measure voltage between all possible configurations of the eight contacts in our sample. We built this set-up to be able to extract the values of the EHE from the Hall Effect measurements, as explained in Chapter 3.3.2.

We used the Keithley 7001 Switch System to open and close the channels and injected current and measured voltage using Keithley 2400 Source-Meter and Keithley 2182 Nanovoltmeter. We also used the Keithley 2400 model to inject current pulses with a minimum duration of 20ms.
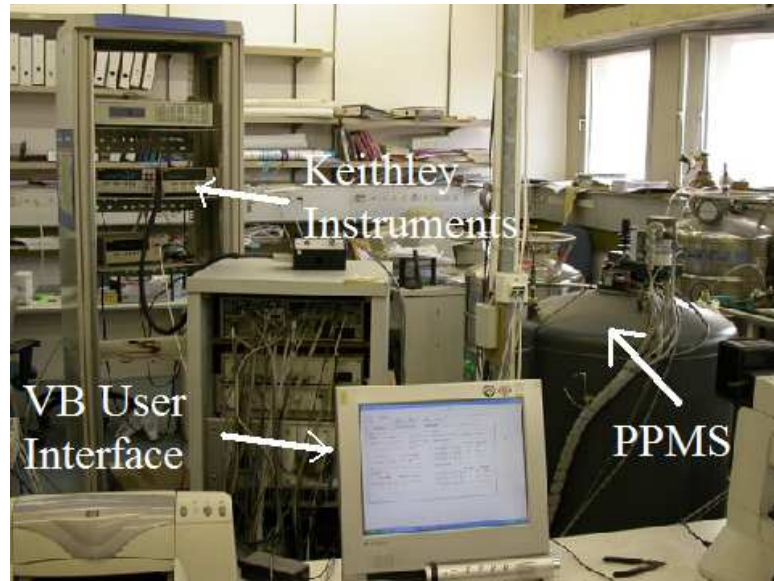
Figure 3.6: The measurement system consisted of QD PPMS, Keithley 2400 source-meter, Keithley 2187 Nanovoltmeter, Keithley 7001 Multiplexer and VB user interface.

3.3.2 Measuring technique

The magnetic state of an SrRuO$_3$ sample was monitored by measuring the EHE between terminals CD and EF (Figure 3.2b).

To determine the EHE, it is necessary to distinguish between different contributions to the Hall effect. Since there is always a small misalignment between the pair of voltage contacts when the transverse resistance is measured (Figure 3.7), the longitudinal resistance also contributes to the measured values. The total resistance measured between terminals C and D can be written as

$$R_{CD} = R_{longitudinal} + R_{transverse} = R_s + R_{as} \tag{3.1}$$

where R_s and R_{as} are symmetric and antisymmetric components of the resistance under the magnetic field reversal. $R_s = R_{MR} + R_{PHE}$, where R_{MR} is magnetoresistance
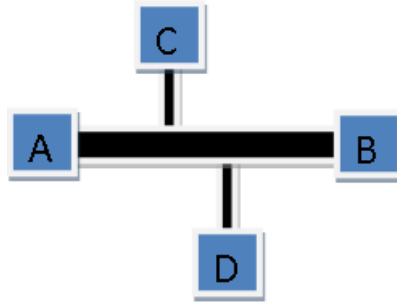
Figure 3.7: Schematic picture of the EHE measurement.

and R_{PHE} is the Planar Hall Effect, and $R_{as} = R_{OHE} + R_{EHE}$, where R_{OHE} is the Ordinary Hall Effect and R_{EHE} is the Extraordinary Hall Effect.

In the case of magnetic field reversion, the expression for R_{CD} can be written as

$$R_{CD}(H) = R_s(H) + R_{as}(H)$$
$$R_{CD}(-H) = R_s(H) - R_{as}(H)$$
$$(3.2)$$

and the symmetric and the anti-symmetric components of the resistance can be written as

$$R_s(H) = \frac{R_{CD}(H) + R_{CD}(-H)}{2}$$
$$R_{as}(H) = \frac{R_{CD}(H) - R_{CD}(-H)}{2}$$
$$(3.3)$$

The reciprocity relation states that $R_{kl,mn}(H) = R_{mn,kl}(-H)$ (where the first two indices indicate current contacts and the second pair denote potential contacts), namely the resistance measured in the presence of the magnetic field H is equal to the resistance measured in the presence of the magnetic field $-H$, if the reversal of the field is accompanied by an exchange in the role of the current and voltage leads [41]. According to this relation, the expressions for R_s and R_{as} can be rewritten as

$$R_s = \frac{R_{AB,CD} + R_{CD,AB}}{2}$$
$$R_{as} = \frac{R_{AB,CD} - R_{CD,AB}}{2}$$
$$(3.4)$$

Since our measurements of the EHE were performed at zero applied field and the self-field of $SrRuO_3$ is very small (see Chapter 2.1.4), the contribution of the OHE to R_{as} can be neglected. We then obtained the values of the EHE by measuring $R_{AB,CD}$ and $R_{CD,AB}$, and calculating

$$R_{EHE} = \frac{R_{AB,CD} - R_{CD,AB}}{2} \tag{3.5}$$

In our measuring system the exchange between current and voltage contacts was performed using the Keithley 7001 Switch System.

In order to exclude the contribution of the contact resistance (Δ) from our results, we performed each resistance measurement twice, and each time we changed the direction of the current. Since (Δ) does not depend on the direction of the current, and from basic symmetry of the Ohm's law $V_{AB,CD} = -V_{BA,CD}$, we were able to exclude the contribution of the contact resistance by calculating the voltage between terminals C and D as

$$V_{CD} = \frac{(V_{AB,CD} + \Delta) - (V_{BA,CD} + \Delta)}{2} \tag{3.6}$$

Chapter 4

Manuscripts

4.1 Efficient current-induced domain-wall displacement in SrRuO$_3$

4.2 Current-induced magnetic instability in SrRuO$_3$

4.3 Suppression of the superconducting critical current of Nb in bilayers of Nb/SrRuO$_3$

Appendix A

Photolithography Recipe

1. **Plasma Cleaning:** Air plasma in the Plasma Cleaner at high power for 20 minutes (it is optional step, to remove a heavy dirt or the residue of Photoresist).

2. **Ultrasonic Bath Cleaning:** Acetone 2-5 minutes, Isopropanol 2-5 minutes.

3. **Microscope Inspection:** Inspection for the cleanliness of the sample.

4. **Spin Coating:** Microposit photoresist S1813, Spinner $5000 rmp$ for 60 seconds.

5. **Pre-Backing:** $120^o C$ on hotplate for 1 minute.

6. **Exposition:** UV light for 7 seconds.

7. **Development:** Developer MF319 for 2 minutes.

8. **Microscope Inspection:** Inspection of the quality of patterning and development.

9. **Post-Backing:** $120^o C$ on a hotplate for 15 minutes.

10. **Post Processing:** Etching in the Gatan HPECS. Voltage $3.7 - 3.9 KeV$, current $150 - 180$ ^1A. Approximate etching rate $100 Å$=min.

LIFT-OFF PROCESSING

1. **Plasma Cleaning:** Air plasma in the Plasma Cleaner at high power for 20

minutes (it is optional step, to remove a heavy dirt or a residue of Photoresist).

2. **Ultrasonic Bath Cleaning:** Acetone 2-5 minutes, Isopropanol 2-5 minutes.

3. **Microscope Inspection:** Inspection of the cleanliness of sample.

4. **Spin Coating:** Negative Photoresist ma-N 405, $5000 - 6000 rmp$ for 60 seconds.

5. **Pre-Backing:** $150^o C$ on a hotplate for 1 minutes.

6. **Exposition:** UV light for 18.5 seconds.

9. **Post-Backing:** $100^o C$ on a hotplate for 1 minutes.

7. **Development:** Developer RD6 for 3.5 seconds.

8. **Microscope Inspection:** Inspection of the quality of patterning and the development.

9. **Post Backing:** $150^o C$ on hotplate for 15 minutes.

10. **Post Processing:** Deposition of Co or Nb.

11. **Photoresist removing:** Remover RR4 or Acetone in the ultrasonic bath for 15 minutes at room temperature.

Appendix B

E-beam lithography Recipe

STEP 1 (1000x1000 μm)

1. **Plasma Cleaning:** Air plasma in the Plasma Cleaner at high power for 30 minutes (it is optional step, to remove a heavy dirt or the residue of PMMA).

2. **Ultrasonic Bath Cleaning:** Acetone 2-5 minutes, Isopropanol 2-5 minutes.

3. **Microscope Inspection:** Inspection of the cleanliness of the sample.

4. **Spin Coating:** 495PMMA A-11 (width 1 μm), Spinner $5000 - 6000 rmp$ for 50 seconds.

5. **Pre-Backing:** $180^o C$ on hotplate for 90 seconds.

6. **Exposition** (Reith):

a. Beam alignment (on Chessy).

b. Write field alignment (on Chessy).

c. Beam focus with magnification x50 (on sample).

d. Exposition: Acceleration Voltage $30 kV$, Current Medium 8, Focus 6, Step Size $0.016 \mu m$, Dose 320 $\mu As/cm^2$.

7. **Development:** MIBK-IPA (1:3) for 30 seconds at room temperature.

8. **Rinsing:** Isopropanol for 15 seconds (to stop development).

9. **Drying:** Nitrogen spray.

8. **Microscope Inspection:** Inspection of the quality of patterning.

STEP 2 (100x100 μm)

1. **Exposition** (Reith):

a. Beam alignment (on Chessy).

b. Beam focus with magnification x500 (on sample).

c. Focus on crosses of the 1000x1000 layer.

d. Exposition: Acceleration Voltage $20kV$, Current Medium 8, Focus 6, Step Size $0.02\,\mu m$, Dose $200 - 240\,\mu As/cm^2$.

2. **Development:** MIBK-IPA (1:3) for 30 seconds at room temperature.

3. **Rinsing:** Isopropanol for 15 seconds (to stop development).

4. **Drying:** Nitrogen spray.

5. **Microscope Inspection:** Inspection of the quality of patterning.

6. **Post Processing:** Etching in the Gatan HPECS. Voltage $3.7 - 3.9KeV$, current $150 - 180\,\mu A$. Approximate etching rate $\sim 100\overset{\circ}{A}/min$.

7. **Removing PMMA:** in Acetone in the ultrasonic bath for 15 minutes at room temperature, then in the air plasma in the Plasma Cleaner at high power for 30 minutes.

Appendix C

KeithleyPPMS Software User Manual

The KeithleyPPMS (KPPMS) software (also known as "Michael's program") was created to perform measurements of the electric transport and of the Hall effect using Keithley Model 2400 Source-Meter, Keithley Model 2182 Nanovoltmeter, Keithley Model 7001 Switch System and Quantum Design PPMS (Figure C.1). This program enables the injection of an electric current and measurement of the voltage between every eight contacts connected to our sample. All the instruments communicate in real time through the GPIB protocol. The KPPMS software consists of more than 5000 lines of computer code programmed on Microsoft Visual Basic 6. I created this software with the assistance of my colleague, Yosi Bason.

Measure DC Voltage

1. Choose DC option in the *Mode* box.

2. Enter the value of the output current in the *Source* box at the *DC Current* menu.

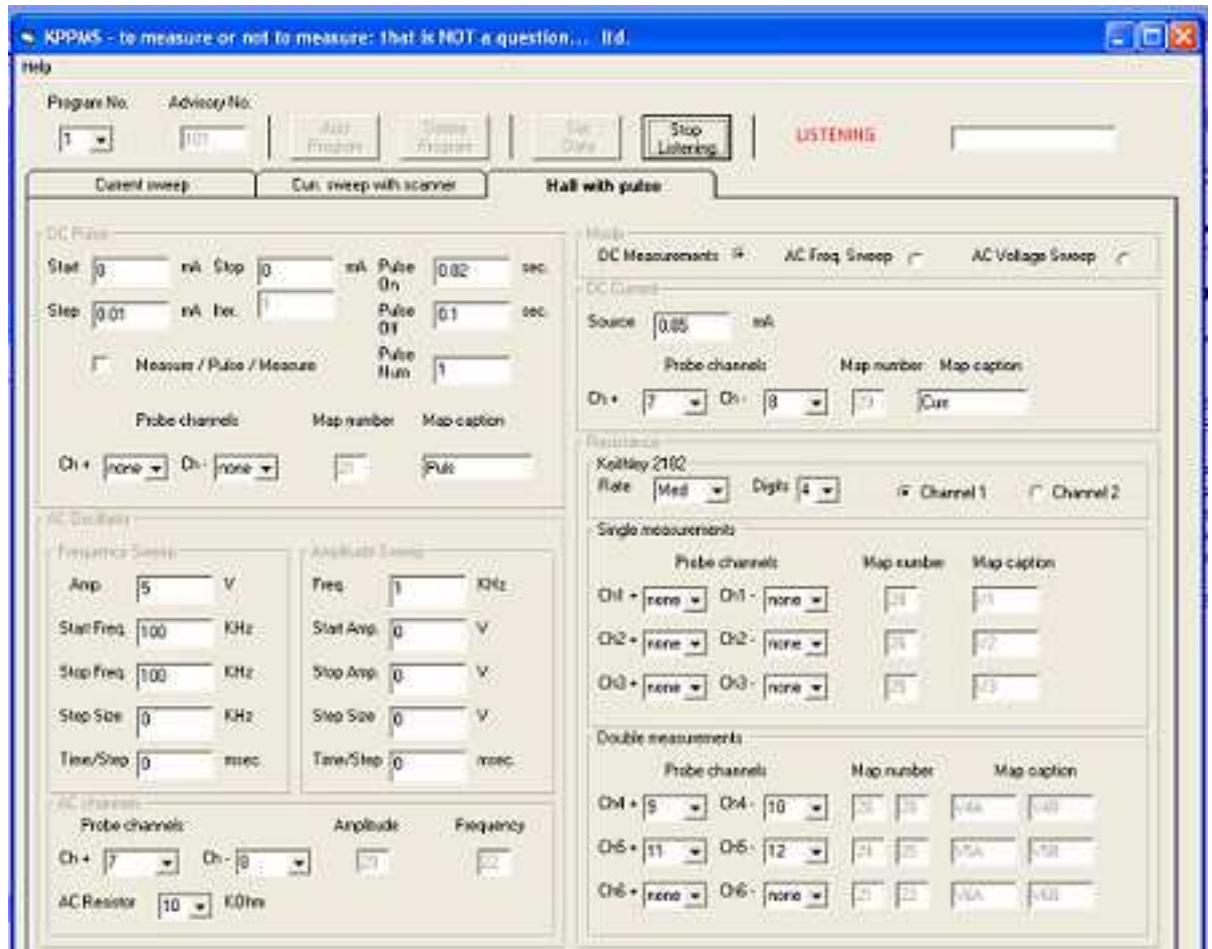3. To inject current pulses before each measurement, choose *Probe channels* at

Figure C.1: KPPMS software user interface.

the *DC Pulse* menu. To inject the pulses before and after each measurement select *Measure/Pulse/Measure* box. Set the property of the pulse by entering *Pulse On*, *Pulse Off* and *Pulse Num* values.

4. Choose the *Probe channels* at the *Single* and/or the *Double measurements* menu. The *Single measurement* designates a voltage measurement between + and − channels. The Double measurement designates a measurement of the Hall effect between two channels according to the procedure described in Chapter 3.3.2. The data of the symmetric term of the Hall effect is stored in the first Map channel and the data of the antisymmetric term is stored in the second Map channel.

5. Press *Set Data* button.

6. To add another measurement programm press *Add Programm* button and enter the details of the measurement.

7. When finished entering the data, press *Start Listening* button. At this point KPPMS is waiting for the *Advisory* command to be sent from the PPMS.

8. Open the MultiVU software and add the *Advice* command in the PPMS sequence file. Set the number of the advice as it appears in the *Advice No.* window at the KPPMS interface. It is important to use the *Upload File* command in the PPMS sequence file to indicate the data file. Figure .... shows the example of the sequence file containing the Advice commands.

In addition to the DC measurements, KPPMS enables the performance of AC measurements using Signal Recovery Lock-In Amplifier and the Keithley Model 7001 Switch System. To convert the Lock-In Amplifier from the voltage source to the

current source we added a variable resistor (R_0) in series to our sample (R_s), when $R_0 >> R_s$. The current in the circuit was approximately calculated as $I = \frac{V_{in}}{R_0}$ and the resistance of the sample was calculated as $R_s = V_s \cdot \frac{R_o}{V_{in}}$.

Measure AC Voltage

1. Choose *AC Freq. Sweep* or *AC Voltage Sweep* option in the *Mode* box.

2. Enter values for *Start*, *Stop*, *Step* and *Time of Step* for the amplitude or the frequency sweep at the *AC Oscillator* menu.

3. Choose the *Probe channels* at the *Double measurements* menu. The resistance value will be stored in the first Map number and the phase value will be stored in the second Map number.

4. Press the *Set Data* button.

5. To add another measurement programm press the *Add Programm* button and enter the details of the measurement.

6. When finished entering all the data, press the *Start Listening* button.

Bibliography

[1] B.D. Cullity, Introduction To Magnetic Materials (1972), Chapter 4.

[2] M. Baibich, J. Broto, A. Fert, F. v. Dau, F. Petroff, P. Etienne, G. Greuzet, A. Friederich, and J. Chazelas, Phys. Rev. Lett. 61, 2472 (1988).

[3] G. Binash, P. Grunberg, F. Saurenbach, and W. Zinn, Phys. Rev. B 39, 4828 (1989).

[4] S. P. Parkin, Z. G. Li, and D. J. Smith, Appl. Phys. Lett. 58,2710(1991).

[5] D.B. Jan, J.Y. Coulter et.,al., App. Phys. Lett. 82, 778, (2003).

[6] J. C. Slonczewski, J. Magn. Magn. Mater. **159**, L1 (1996).

[7] J.A. Katine *et al.*, Phys. Rev. Lett. **84**, 3149 (2000).

[8] E.B. Myers, D.C. Ralph, J.A. Katine, R.N. Louie, R.A. Buhrman, Sience **285**, 867 (1999).

[9] M.Tsoi *et. al.*, Phys. Rev. Lett. **80**, 4281 (1998).

[10] J.Grollier *et. al.*,Appl. Phys. Lett. 78, 3663 (2001).

[11] L. Berger, J. Appl. Phys. **55**, 1954 (1984); **71**, 2721 (1992).

[12] M. Klaui, C. A. F. Vaz, J. A. C. Bland, W. Wernsdorfer, G. Faini, E. Cambril, L. J. Heyderman, Appl. Phys. Lett. **83**, 105 (2003).

[13] A. Yamaguchi, T. Ono, S. Nasu, K. Miyake, K. Mibu, T. Shinjo, Phys. Rev. Lett. **92**, 077205 (2004).

[14] J. Grollier, P. Boulenc, V. Cros, A. Hamzi, A. Vaures, A. Fert, and G. Faini, Appl. Phys. Lett. **83**, 509 (2003).

[15] C. K. Lim, T. Devolder, C. Chappert, J. Grollier, V. Cros, A. Vaures, A. Fert , and G. Faini, Appl. Phys. Lett. **84**, 2820 (2004).

[16] N. Vernier, D. A. Allwood, D. Atkinson, M. D. Cooke and R. P. Cowburn, Europhys. Lett. **65**, 526 (2004).

[17] L.Gan, S.H. Chung, K.H Aschenbach, M. Dreyer and R.D. Gomez, IEEE Transaction on Magnetism **36**, 3047 (2000).

[18] M. Yamanouchi, D. Chiba, F. Matsukura, and H. Ohno, Nature **428**, 539 (2004)

[19] M. Feigenson, J.W. Reiner, L. Klein, Phys. Rev. Lett. **98**, 247204 (2007).

[20] M. Laufenberg, W. Buhrer, D. Bedau, P.-E. Melchy,1 M. Klaui, L. Vila, G. Faini, C. A. F. Vaz, J. A. C. Bland, and U. Rudiger, Phys. Rev. Lett. **97**, 046602 (2006).

[21] M.Hayashi, L. Thomas, Ya.B. Bazaliy, C. Rettner, R. Moriya, X. Jiang, S.S.P. Parkin, Phys. Rev. Lett. **96**, 197207 (2006).

[22] G. Tatara, H. Kohno, Phys. Rev. Lett. **92**, 086601 (2004).

[23] J. Shibata, G. Tatara, H. Kohno, Phys. Rev. Lett. **94**, 076601-1 (2005).

[24] J.W. Wegroew, D. Kelly, Y. Jaccard, Ph. Guittienne, J.Ph. Ansermet, Europhys. Lett. **45**, 626 (1999).

[25] Y. Ji., C.L. Chien, M.D. Stiles, Phys. Rev. Lett. **90**,106601 (2004).

[26] T.Y. Chen, Y.Ji., C.L. Chien, M.D. Stiles, Phys. Rev. Lett. **93**, 026601 (2004).

[27] D. Chiba, Y. Sato, T. Kita, F. Matsukura, H. Ohno, Phys. Rev. Lett. **93**, 216602 (2004).

[28] M. Feigenson, J.M Reiner, L. Klein, J. App. Phys. to be published (2008).

[29] Sonin

[30] L. N. Bulaevskii, E.M. Chudnovsky et. al., App. Phys. Lett. 76, 2594 (2000).

[31] Introduction to Superconductivity. M.Tinkham.

[32] L. Klein, J.S. Dodge, C.H. Ahn, J.W. Reiner, L. Mieville, T.H. Gaballe, M.R. Beasley and A. Kapitulnik, J.Phys. Condens. Matter 8, 10111 (1996)

[33] Griffit, The Theory of Transition Metal Ions (Cambrige University Press) p 113, 1961.

[34] Emery V J and Kivelson S A, Phys. Rev. Lett. 74, 3253 (1995).

[35] L. Klein, J.R. Reiner, T.H. Geballe, M.R. Beasley, A. Kapitulnik, Physica B 281, 608-609 (2000).

[36] G. Santi amd T. Jarlborg, J.Phys Condens. Metter **9**, 9563 (1997).

[37] F. Marshall *et. al.*, J. Appl. Phys. **85**, 4131-4140 (1999).

[38] I Asulin, O.Yuli ,G. Koren, O. Millo, Phys Rev bf 74, 092501 (2006).

[39] L. Klein,Y. Kats, A. F. Marshall, J. W. Reiner, T. H. Geballe, M. R. Beasley, A. Kapitulnik., Phys. Rev. Lett. **84**, 6090-6093.

[40] M.Tinkham, Introduction to Superconductivity.

[41] M. Buttiker, Phys. Rev. Lett. **57**, 1761 (1986).